Chapter 3. An X-ray Detection System

3.1 Configuration of The Prototype Scanning System

A number of factors that influence the measured intensity of an x-ray image have been briefly discussed in Chapter 2. First, the image that is acquired by detector depends on the spectral distribution of the x-ray source. The individual objects are characterized by their material properties, such as atomic composition, density, and thickness. The detector converts x-ray photons to visible light photons and then photodiode converts the visible photons to electrical current that is amplified and sampled, forming the final image. An x-ray imaging system is usually built up based on the factors above.

The purpose of this chapter is to present a x-ray imaging system, which was built up at the SDA lab of Virginia Tech, and a model of this x-ray imaging system. The model is important for system analysis, simulation, and design.

3.1.1 AS&E 101zz x-ray machine

The major x-ray source and sensor components of the prototype system developed at the SDA lab of Virginia Tech were obtained from an AS&E 101zz luggage inspection system [AME82] [AME86]. The AS&E 101zz system is configured to obtain a single transmission

image and two back scattering images. Two x-ray sources are used, one for each side of the bag. The first x-ray source and detectors create back scattering and transmission images for one side of the bag. Then the second x-ray source and detectors collect only a back scattering image for the other side of the bag.

The AS&E 101zz luggage inspection system uses a collimator and chopper wheel to transform the conical beam of the x-ray source into a "flying spot" (see Figure 3.1-1. The x-ray source assembly consists of an x-ray tube in one housing and a chopper wheel in another housing. These two housings are connected by a triangularly shaped structure through which the beam passes, as it goes from the x-ray tube to the chopper wheel.

The x-ray tube generates the x-rays, which emanate from the tube mouth in a conical shape. Most of these x-rays are absorbed in the housing and pre-collimators, leaving a rectangular beam passing through the triangular connecting structure. At the wheel end of this structure, there is a stationary slit collimator that sharpens the beam into a clean rectangular slit shape. This is the beam shape as it passes into the wheel housing and impinges on the rear of the wheel. The wheel has a lead annular ring and four radial slits, 90 degrees apart. As the wheel turns, one end of these radial slits enters the rectangular slit beam, allowing a small amount of x-rays to pass (a parallelogram in cross section). As the radial slit progresses, the small spot of x-rays passes upward until the end of the slit passes beyond the stationary slit, and all x-rays are again cut off until another radial slit enters the beam at the bottom.

This x-ray spot repeatedly scans the x-ray inspection area in a vertical direction, allowing the use of a single large area sensor for each detector, instead of an array of pixilated sensor elements. These sensors are interfaced with digitizing boards. Each digitizing board creates successive 1-dimensional slices of a scanned object that are appended together to create a 2-dimensional image.

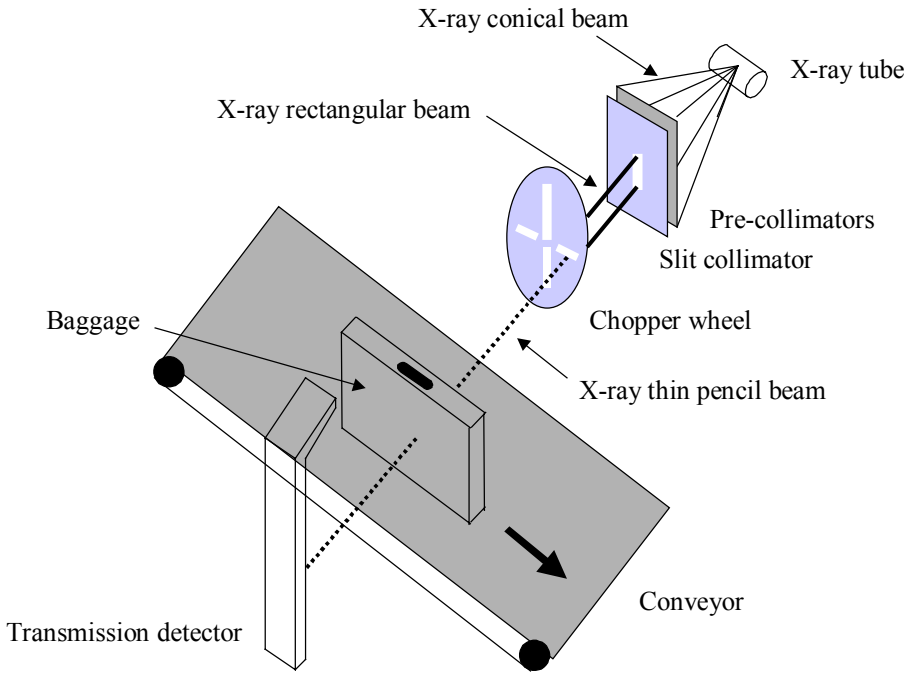

Figure 3.1-1 Schematic diagram of "flying spot" in AS&E 101zz. It mainly consists of, (1) x-ray tube, (2) pre-collimators, (3) slit collimator, (4) chopper wheel, (5) conveyer, and (6) detectors. Only a transmission detector is shown in the diagram.

3.1.2 Configuration of the prototype scanning system

An AS&E 101zz x-ray scanning system has been modified to suit the needs of the Virginia Tech research effort in exploring the feasibility of combining multi-energy and scattered x-ray imaging technologies. One goal is to improve the material characterization capabilities of this combination of technologies through system optimization, simulations, and experimental tests. Most work of this dissertation is related with this effort. A second goal is to develop image processing algorithms to determine the true x-ray intensities of objects that overlap. Finally, a prototype multi-energy and scatter x-ray imaging system has been developed to simultaneously collect and process high-resolution images, using the new algorithms mentioned above.

The prototype x-ray scanning system was constructed by modifying an AS&E 101zz (see Figure 3.1-2). It is characterized by the following [CON96]:

(1) To investigate forward scattering images, the second back scattering detectors have been moved forward to the first x-ray source. Both the sensing elements and the digitizing board have been moved forward, eliminating the need for the second source.
(2) To obtain the transmission images at two different energies with a single x-ray source, a copper filter has been introduced and an "active" scanning method is used. The term "active" in the prototype scanning system means that at least three operations are performed. 1) Based on the operator's option, an interface board can control the conveyer to move forward, then backward, and then forward again. 2) A stepper motor causes the copper filter to move up and down. 3) The high voltage power supply to x-ray tube is automatically switched

between two designated values (so-called high energy and low energy). The introduction of the copper filter is to reduce the x-ray source spectrum overlap and output signal imbalance between high energy and low energy sensing.

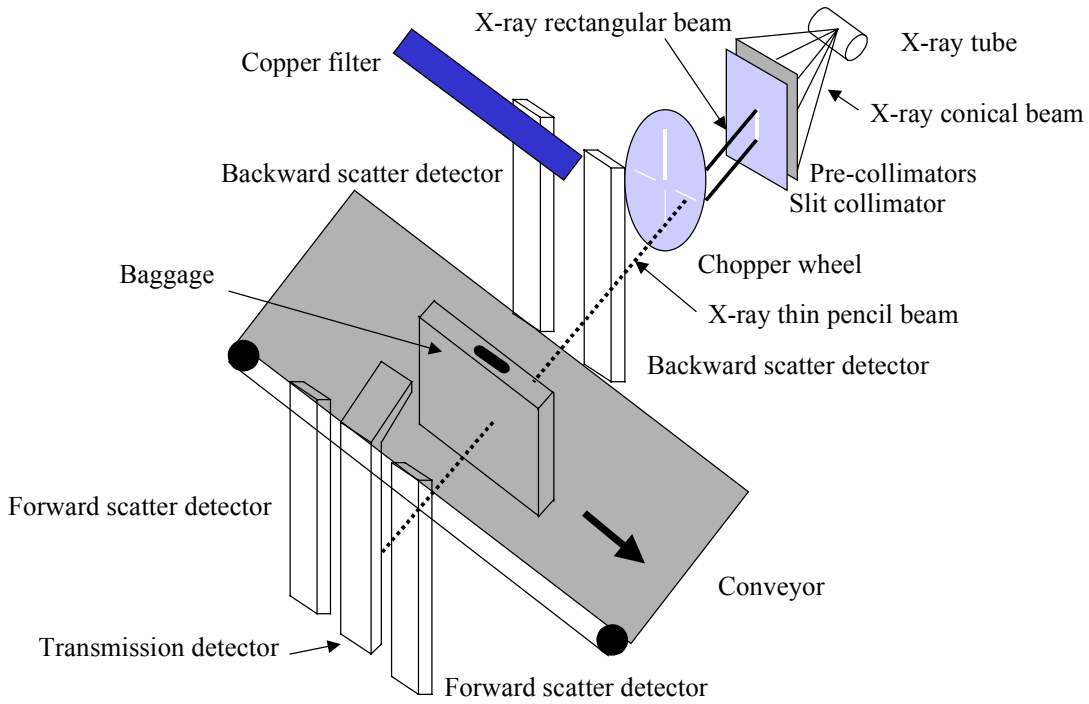

Figure 3.1-2 Schematic geometry of the prototype image sensors and source. There are two main modifications on the AS&E 101zz: (1) one backward scatter detector is used as forward scatter detector; and (2) a copper filter is inserted for collecting dual energy transmissions.

(3) To meet the research requirements on simulations and experimental study, new data collection and processing hardware have been incorporated into the system. Three electronic hardware components are used in the prototype system for data collection and real-time processing. Each of these components is constructed using Field Programmable Gate Array (FPGA) chips for flexibility and reconfigurability. These boards are called the Differential Pair Interface Board (DPIB), the Modular Reprogrammable Real-time Processing Hardware (MORRPH) board, and a Multiple Channel PCI (MCPCI) bus master data collection board. These adapter cards are connected with the AS&E 101zz x-ray scanning system through a master host computer. The functions and interconnection of these boards are shown in [DRA98].

(4) To automate the collection of dual-energy images, a prototype user interface has been created to control several components from a master computer. This involves the integration of several optical beam break devices, the motor controller for the conveyor, the stepper motor controller for the copper filter, the x-ray source controller, and the AS&E digitizer boards. The description and implementation of this user interface are described in [ARV97].

3.2 The Prototype Scanner Model

3.2.1 The block diagram of prototype scanner

An x-ray source creates x-rays with an intensity of $I_0(E)$, as shown in the system model of Figure 3.2-1. The x-rays interact with the object being scanned, and can be collected by three detectors: the transmission detector, the backward scatter detector, and the forward scatter detector. The inputs of these three detectors are represented as $I(E)$, $I_B(E)$, and $I_F(E)$,

respectively. Two-dimensional scanning techniques are used in all detectors to get x-ray intensities of the object from pixel to pixel. The signals collected from the detectors are represented by $T(x, y)$, $B(x, y)$ and $F(x, y)$, respectively, where x and y represent the image position in two-dimensional space.

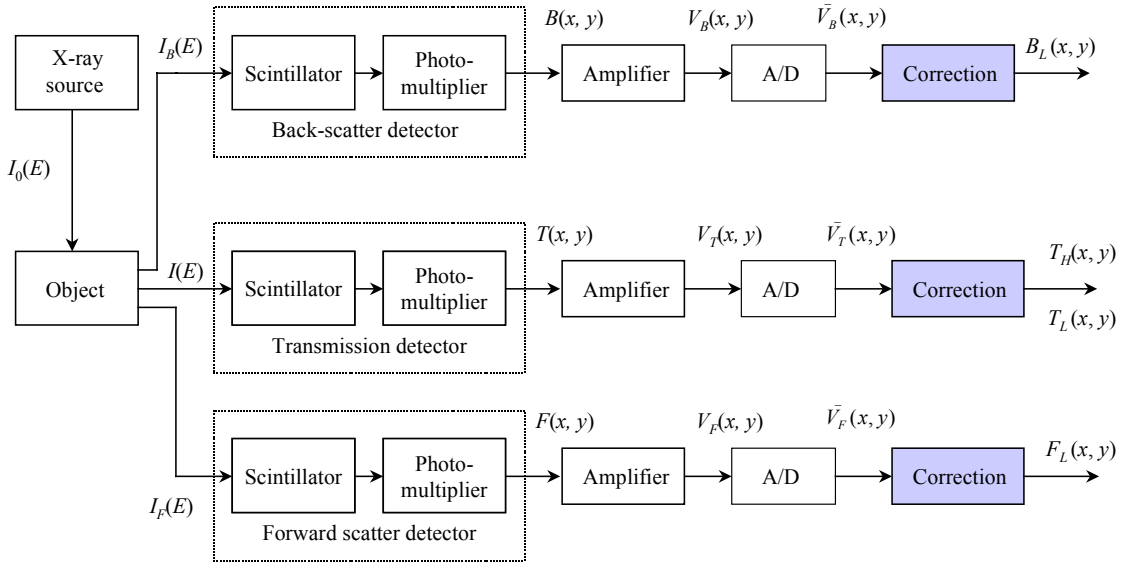

Figure 3.2-1 Block diagram of the prototype scanner. It comprises an x-ray source assembly, scintillation detectors, amplifier circuits, analog-to-digital (A/D) converters, and corrections.

The outputs of the detectors are fed into a set of amplifiers. Each amplifier consists of a log amplifier, an anti-log amplifier, and an integrator. The amplified signals are represented as $V_T(x,y)$, $V_B(x,y)$, and $V_F(x,y)$, respectively. The output signals of the amplifiers are further converted into digital signals through analog-to-digital (A/D) converters. We use

$\bar{V}_T(x,y)$, $\bar{V}_B(x,y)$, and $\bar{V}_F(x,y)$ to represent digital values of transmission, backward scattering and forward scattering images scanned for a certain object.

There exist some variations on the digital values due to the scanning methods used in the prototype scanning system. In this dissertation, we do software corrections to obtain $T_H(x, y)$, $T_L(x, y)$, $B_L(x, y)$, and $F_L(x, y)$. The software corrections have two functions: 1) the amplifier circuit correction, and 2) shading or dark-current correction. They will be addressed in the following sections in detail. Also, the prototype system was developed to be a dual-energy transmission plus scattering system, since only one x-ray source and one transmission detector are installed, the transmission images are collected at two times. The subscripts H and L distinguish the images that are scanned with high and low energy respectively.

3.2.2 X-ray source emission

The x-ray source assembly, which forms the "flying spot" beam for object scanning, comprises two individually housed components: an x-ray tube and a rotating chopper wheel. A wedge shaped structure connects these two component housings.

The x-ray source assembly emits a thin pencil beam with a polychromatic spectrum, which can be simulated with Equation (2.5) as discussed in Section 2.1.2.

3.2.3 Detected signals

For a certain "spot" (x, y), as shown in Figure 3.2-2, every material in the bag along the line of the x-ray beam will contribute to the attenuation of the beam. Because the x-ray beam is not always perpendicular to the detector planes, two coordinate systems are used to describe

the detector plane (x, y, z), and the object plane along the line of x-ray beam (x', y', z'), respectively.

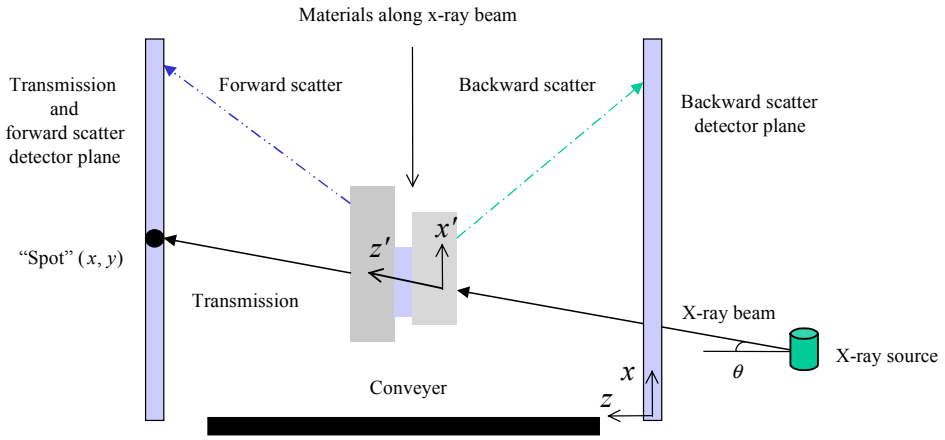

Figure 3.2-2 Coordinate representation of the imaging geometry. The objects being scanned move in the y direction, out of the page.

(1) Transmission signal

For transmission imaging, the photoelectric effect and scattering both contribute to the detected signal, resulting in the following equation [SCH91]:

$$T(x,y) = \int dE\, N(E)\, e^{-\left\{\int dz' \mu_t(x',y',z',E)\right\}} P_d(E)\, E \qquad (3.1)$$

where $T(x, y)$ is the detected transmission signal at the x and y coordinates of the projected image, $N(E)$ is the number of incident x-ray photons between E and $E+dE$, $\mu_t(x', y', z', E)$ is

the total linear attenuation coefficient (cm^{-1}) as measured along the x-ray line of sight, $P_d(E)$ is the detection probability of a photon of energy E incident at the detector, and E is photon energy.

The main integration is over the energy spectrum of the incident radiation. The exponential term represents the attenuation along the line of sight associated with a given pixel for photons at a given energy. The last part of the equation is the detection probability in the transmission detector times the energy of the photon; this is only used in energy sensitive detectors, such as a scintillation detector. In photon counting detectors this energy factor is not present. The transmission signal at any energy depends on the density of the material and on the total linear attenuation coefficient (μ_t) which describes both scattering and absorption.

(2) Backward scattering signal

For back scattering, the estimation of the detected signal $B(x, y)$ is [SCH91]:

$$B(x,y) = \int dE\, N(E) \int dz' \left[e^{-\left\{ \int_0^{z'} dt\, \mu_t(x',y',t,E) \right\}} \right] \left[\sigma_s(E)\, \rho(x',y',z') \right] \cdot \left[\int d\Omega\; e^{-\left\{ \int_z^{0} dt\, \mu_t(x'',y'',t,E) \right\}} \right] P_d(E)\, E \tag{3.2}$$

where the notation is the same as for the transmitted radiation, except $B(x, y)$ is the scattered photon signal at the position (x, y) of the projected image, z' is the depth into the object along the pencil beam at which scattering occurs, $\sigma_s(E)$ is the scattering cross section as a function of energy, $\rho(x', y', z')$ is the density (g/cm^3) of the materials in the bag along the x-ray line of sight, and E' is the photon energy after scattering.

Again the first integral is taken over the incident x-ray spectrum as a function of energy. The next integral is taken along the line of sight in the bag. The scatter signal detected from each depth into the bag is treated differentially. The first term in square brackets describes the attenuation of the beam from the front surface of the bag to the depth z'. The second term in square brackets describes the probability of scatter per photon in the region of the pencil beam from z' to $z'+ dz'$. The third term in square brackets describes the attenuation of the scattered radiation as it travels from the region of scatter to scatter detectors along the line (x'', y'', z'') over the total solid angle of those detectors, and therefore must be integrated over the solid angle Ω subtended by the detectors. The factor $P_d(E')E'$ again represents the detection efficiency for an energy sensitive detector.

(3) Forward scattering signal

The forward scattering signal can be expressed in the similar form as the back scattering signal [SCH91]. Note that as with back scattering, there is an integral over the thickness of the object; however, the second attenuation term is now integrated over the range from z' to D.

$$F(x,y) = \int dE\, N(E) \int dz' \left[e^{-\left\{ \int_0^{z'} dt\, \mu_t(x',y',t,E) \right\}} \right] \left[\sigma_s(E)\, \rho(x',y',z') \right] \cdot \left[\int d\Omega\; e^{-\left\{ \int_{z'}^{t} dt\, \mu_t(x'',y'',t,E) \right\}} \right] P_d(E)\, E \tag{3.3}$$

where the notation is the same as for the transmitted radiation and scattered radiation, except $F(x, y)$ is the scattered photon signal from the position (x, y) of the projected image.

3.2.4 The verification and correction of the amplifier circuit

The amplifier circuit, which consists of log amplifier, anti-log amplifier, and integrator, is intended to operate as a linear amplifier. To the extent that the amplification is not linear, a correction is needed if we want to directly use Equations (3.1), (3.2), (3.3) in the system analysis and design. Two processes therefore are related to this problem. One is called "forward problem" which means to develop a mathematical model for the circuit using measured data. Another is the "inverse problem", where correction is done based on the measured data available and the expression obtained at the first step. The block diagram of the circuit is shown in Figure 3.2-3, where spatial coordinate (x, y) is omitted since the circuit itself is not related to image location. In this figure, i is the applied input to the circuit through adjusting the beam current of x-ray machine, V_1 is the output of the "log" amplifier, V_2 is the output of the "anti-log" amplifier, and finally V is the output of the "integrator".

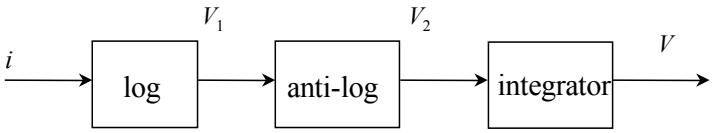

Figure 3.2-3 Block diagram of the amplifier circuit.

(1) Verification of the amplifier circuit

To verify the property of the circuit, the voltage values at various points of transmission imaging were measured with a change of the beam currents (similar to a change in the number of photons). The curve-fitting method is then used to model the circuit. From the circuit definition, the output at each stage can be described follows:

The output of the logarithmic amplifier is assumed to be

$$\tilde{V}_1 = C_0 \ln(i) + C_1 \tag{3.4}$$

where C_0 and C_1 are two unknown constants.

The output of the anti-log amplifier is assumed to be

$$\tilde{V}_2 = A_0 e^{\tilde{V}_1} + A_1 \tag{3.5}$$

where A_0 and A_1 are two unknown constants.

The output of the integrator is assumed to be

$$\tilde{V} = B_0 \tilde{V}_2^{\,2} + B_1 \tilde{V}_2 + B_2 \tag{3.6}$$

where B_0 , B_1 and B_2 are three unknown constants. The measured voltage levels are given in Table 3.2-1.

With the known relationship between input and output of the measured data pairs, a curve-fitting method can be used to calculate the unknown parameters. Without loss of generality, suppose that two parameters, a_1 and a_2, are to be estimated in Equation (3.7),

$$y = a_1 x + a_2 \tag{3.7}$$

The measured outputs are: $Y = [y_1, y_2, \ldots, y_n]^T$ for the given inputs $X = [x_1, x_2, \ldots, x_n]^T$. Let $A = [a_1, a_2]^T$, yielding

Table 3.2-1 Outputs of the amplifier circuit for transmission imaging with no object in the x-ray path.

i (mA)	0.5	1.0	1.5	2.0	2.5	3.0	4.0	5.0
$\tilde{V}_1$ (volts)	-0.80	-0.50	-0.35	-0.20	-0.10	0.00	0.10	0.20
$\tilde{V}_2$ (volts)	0.75	1.50	2.10	2.60	3.05	3.50	4.25	4.75
$\tilde{V}$ (volts)	0.00	1.50	3.00	4.00	5.00	6.00	8.00	9.30

$$A = (Z^T \cdot Z)^{-1} \cdot Z^T \cdot Y \tag{3.8}$$

where $Z = [X \quad U]$, and U is an n-dimensional unit vector. Substituting Table 3.1 into Equation (3.4), (3.5), and (3.6) respectively, we have,

$$\tilde{V}_1 = 0.46 \cdot \ln(i) - 0.55 \tag{3.9}$$

$$\tilde{V}_2 = 5.03 \cdot e^{\tilde{V}_1} - 1.55 = 3.05 \cdot i^{0.46} - 1.55 \tag{3.10}$$

$$\tilde{V} = 0.09 \cdot \tilde{V}_2^{\,2} + 1.51 \cdot \tilde{V}_2 + B_2 = 0.85 \cdot i^{0.92} + 4.62 \cdot i^{0.46} - 3.52 \tag{3.11}$$

Using the above equations, the estimated voltage values are shown in Figure 3.2-4. Let us define the residual error as:

$$e = \sqrt{\frac{1}{n}\sum_{j=1}^{n}\left(V(j) - \tilde{V}(j)\right)^2} \tag{3.12}$$

Substituting the measured voltage values V from Table 3.2-1 and calculated voltage values $\tilde{V}$ from Equation (3.11) into Equation (3.12), it is found that the residual error is about 0.11 volts. So Equations (3.9), (3.10) and (3.11) can be thought as a good model for the amplifier circuit.

(2) Correction of the amplifier circuit

Through the above verification of the amplifier circuit, we know that output of the circuit V, which is provided directly by the prototype scanner, is not exactly a linear function of the circuit input i. To decrease the error due to directly using expressions of the x-ray source and the detected signals, i.e., Equations (3.1), (3.2), (3.3), and (3.4), in our system analysis and simulations, a consideration on this non-linearity is indispensable. The algorithm is given as follows:

♦ *Algorithm 3.1*

(i) For a measurement, $V(x, y) \in \{V_T(x, y), V_B(x, y), V_F(x, y)\}$, find the corresponding value $i \in \{T(x, y), B(x, y), F(x, y)\}$ with Equation (3.11);

(ii) Repeat above step for all pixels in one image.

The algorithm above can be directly applied to the digital values $\bar{V}(x,y) \in \left\{\bar{V}_T(x,y), \bar{V}_B(x,y), \bar{V}_F(x,y)\right\}$ because of one-to-one linear mapping characteristic of analog-to-digital converters.

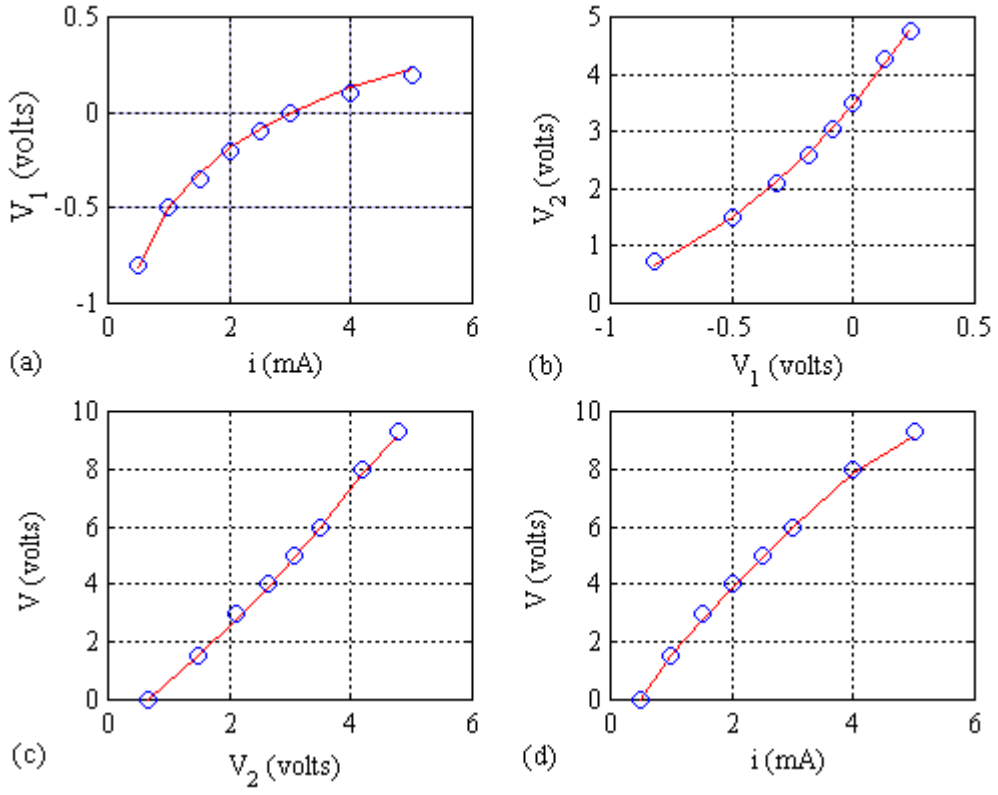

Figure 3.2-4 Comparison of the measured voltages (circles) and calculated voltages (solid lines): (a) output of log amplifier; (b) output of anti-log amplifier; (c) output of integrator; (d) overall output of the amplifier circuit.

3.2.5 Shading correction

The defects in x-ray images may be present due to an imperfect x-ray source or non-uniform detectors. In the prototype scanning system, an x-ray source with a thin soft-ray filter can be made quite good, but the photo-multiplier tubes (PMT) used in the detector introduce two problems, namely non-uniformity and dark current, which have to be corrected.

(1) Photo-multiplier-tubes

The photo-multiplier tube consists of a photo-cathode, an anode and about 10 intervening dynodes at which the electron multiplication take place. The photo-cathode material is chosen to have high quantum efficiency and low thermionic emission. The quantum efficiency of a photo-cathode is sometimes referred as the radiant cathode sensitivity $\varepsilon(\lambda)$, and is given by [MIC93],

$$\varepsilon(\lambda) = \frac{I_K}{P(\lambda)} \tag{3.13}$$

where I_K is the photoelectric emission current and $P(\lambda)$ is the incident radiant power.

Most metals are not suitable as photo-cathodes because photoelectrons released from atoms will collide with free conduction-band electrons and transfer their energy. Only a few electrons will have sufficient energy to overcome the surface potential. Semiconductors have

far fewer free electrons than metals and so photoelectrons suffer fewer collisions, resulting in quantum efficiency about two orders of magnitude higher than those of metals. Most photo-cathode materials are usually formed from a combination of antimony and one or more alkali metals.

Electrons released from a photo-cathode drift across to the first dynode, and the electron pulse then impinges on successive dynodes and finally reaches the anode. For maximum efficiency, all photoelectrons must reach the first dynode and they should have the same time of flight so that a fast uniform secondary-yield pulse is produced. This can be helped by the use of focusing and accelerating electrodes. But even though electron optics are well formed, there is a transit time variation, Δt, due to the range of speeds with which photoelectrons leave the photo-cathode. Total transit times are typically a few tens of nanoseconds.

Possible dynode configurations are shown in Figure 3.2-5. Venetian blind and box and grid systems have large dynode areas and efficiently collect photoelectrons. However, these systems have a considerable spread in the transit time, and they are not suited to fast scintillators. They can be used with NaI(Tl), which has a luminescence decay of one microsecond. Linear and circular focused systems are good for fast timing applications such as particle detection, where time resolution is more important than pulse-height spread. Micro-channel plate systems are of good time responses and are almost unaffected by magnetic fields. They, however, have a poor dynamic range and show poor linearity as a function of output current.

The photo-multiplier requires potentials of hundreds volts between the photo-cathode and the first dynode, and between adjacent dynodes. These voltages are normally produced from a potential divider located within the photo-multiplier housing and connected to a positive dc supply in the region of thousand volts. The anode is returned to the supply through an anode load, and is connected to the input of a cathode follower.

The multiplication factor β of a dynode depends on the nature of the surface and on the energy of the incident electrons. For a SbCs dynode, with inter-dynode potential V_{id}, β may be approximated by [SHA58],

$$\beta \approx 0.2 \cdot V_{id}^{0.7} \tag{3.14}$$

For a photo-multiplier with a chain of n dynodes, the total gain G is,

$$G = \beta^n \approx \left(0.2 \cdot V_{id}^{0.7}\right)^n \tag{3.15}$$

To achieve uniform gain, it is very important to keep V_{id} constant, and it is for this reason that capacitors and zener diodes are often placed across the last few stages.

In the absence of any radiation striking the photo-cathode, some current is still produced. This is due to thermionic emission from the cathode and the dynodes, leakage currents from material between the electrodes, radioactive contamination of ion feedback at high tube currents. The dominant background is thermionic noise. The thermionic dark current I_{DT} at temperature T is given by the Richardson-Dushman equation [MIC93],

$$I_{DT} = A \cdot S \cdot T^2 \cdot e^{-e\phi/kT} \tag{3.16}$$

where k is Boltzmann's constant, A is a constant depending on the material, S is the area of the emitting surface and ϕ is the work function of the material. For most photo-multipliers, dark currents are about a few nanoamperes.

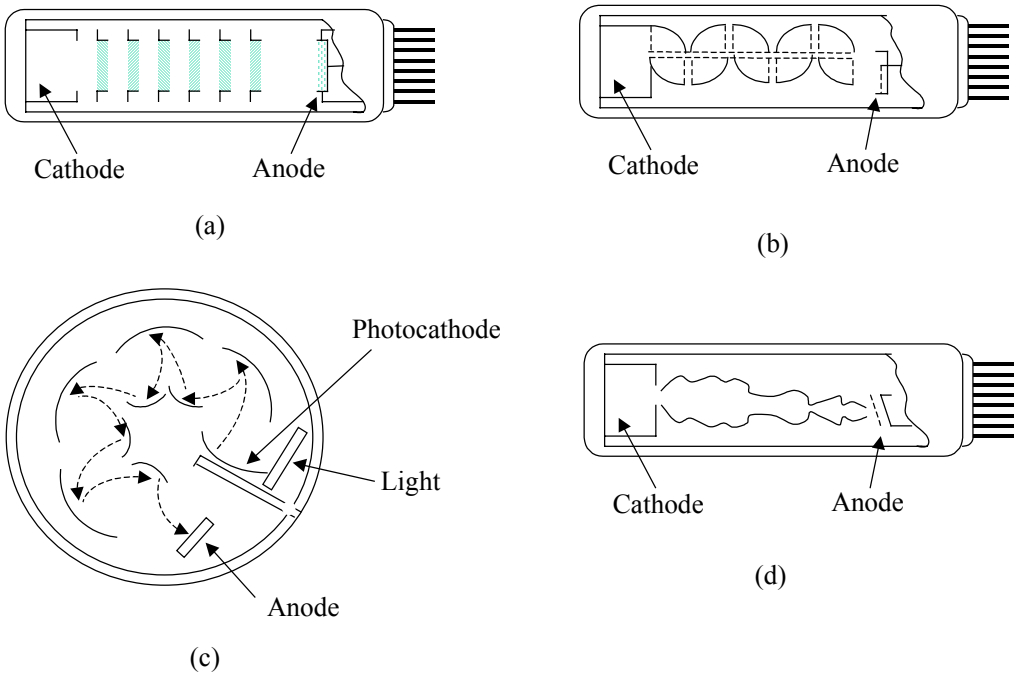

Figure 3.2-5 Common photo-multiplier structures: (a) Venetian blind, (b) box and grid, (c) side-on circular focus and (d) linear focused.

(2) PMT in the prototype scanner

The PMT used in the prototype scanner has a box-and-grid structure. There are eight stages of dynodes, and the secondary-emitting surface is made of alkali-antimonide. The photo-cathode material is semi-transparent KCsSb. This PMT has a variable current amplification gain which ranges from, for example, 2×10^5 to 8×10^5 at 1000 volts power supply [BUR96]. For transmission imaging, four PMTs are mounted in the detector, and intensity variations are produced spatially in the image because x-ray beams focus in a certain directions onto particular PMTs (see Figure 3.2-6a). Statistical analysis shows that the standard deviation for this non-uniformity is about 16 intensity values. Correcting these intensity variations is known as "shading correction". For scatter imaging, there is no such a problem due to x-ray diffusion and the signal integration on all space angles, but the dark currents still exist. The average dark currents are about 25 intensity values for backward scattering image (see Figure 3.2-7a), and 18 intensity values for forward scattering image (see Figure 3.2-8a).

These defects can be corrected if they remain unchanged over some period of time, which has been verified through hundreds of measurements in SDAL. After shading correction, the standard deviation of intensity variations for the transmission images decreases to 3 intensity values. One example is given in Figure 3.2-6b. The algorithm used to correct the transmission image is independent on the image scanned at high or low energies, and is given as follows:

♦ *Algorithm 3.2*

(i) Collect the "background" transmission image $\bar{V}_{T0}(x,y)$ with size of n rows and m columns;

(ii) For x = 1 to x = n, calculate the mean value $a(x)$ for each row x by using $a(x) = \frac{1}{m}\sum_{y=1}^{m} \bar{V}_{T0}(x,y)$;

(iii) Collect the transmission image $\bar{V}_T(x,y)$ with size of n rows and k columns;

(iv) For x = 1 to x = n, correct $\bar{V}_T(x,y)$ for each row x by using $T(x,\ 1:k) = \bar{V}_T(x,\ 1:k) \Big/ a(x)$.

The corrected scattering images have only a dark current of 3 intensity values on the average, as shown in Figures 3.2-7b and 3.2-8b. The algorithm is as follows:

♦ *Algorithm 3.3*

(i) Collect the "background" scatter image $\bar{V}_{S0}(x,y) \in \left\{\bar{V}_{B0}(x,y), \bar{V}_{F0}(x,y)\right\}$, with size of l rows and m columns;

(ii) Calculate the mean value s for $\bar{V}_{S0}(x,y)$;

(iii) Collect scatter image $\bar{V}_S(x,y) \in \left\{\bar{V}_B(x,y), \bar{V}_F(x,y)\right\}$ with size of l rows and k columns;

(iv) For each pixel, correct $\bar{V}_S(x,y)$ to obtain $S(x,y) \in \{B(x,y), F(x,y)\}$ by using $S(1:l,\ 1:k) = \bar{V}_S(1:l,\ 1:k) - s$.

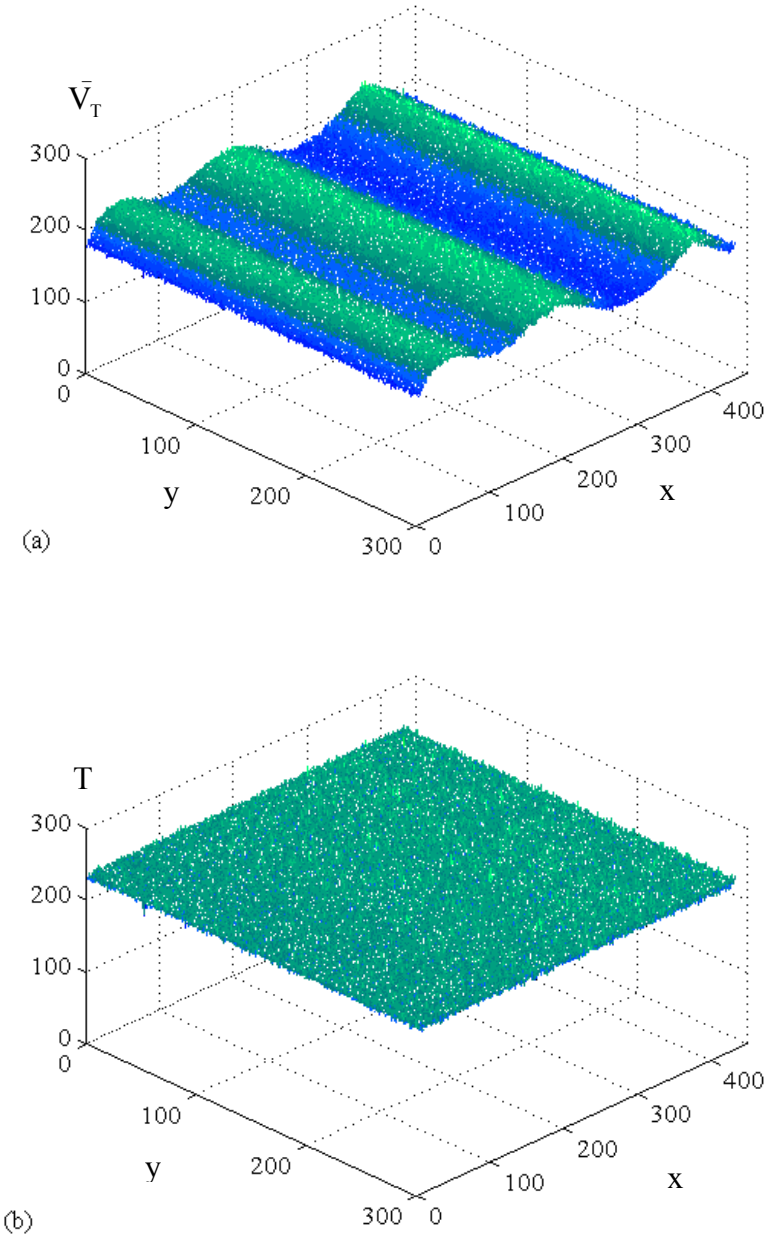

Figure 3.2-6 Non-uniformity of the transmission image: (a) before shading correction, (b) after shading correction; where *y* is the column index and *x* is the row index.

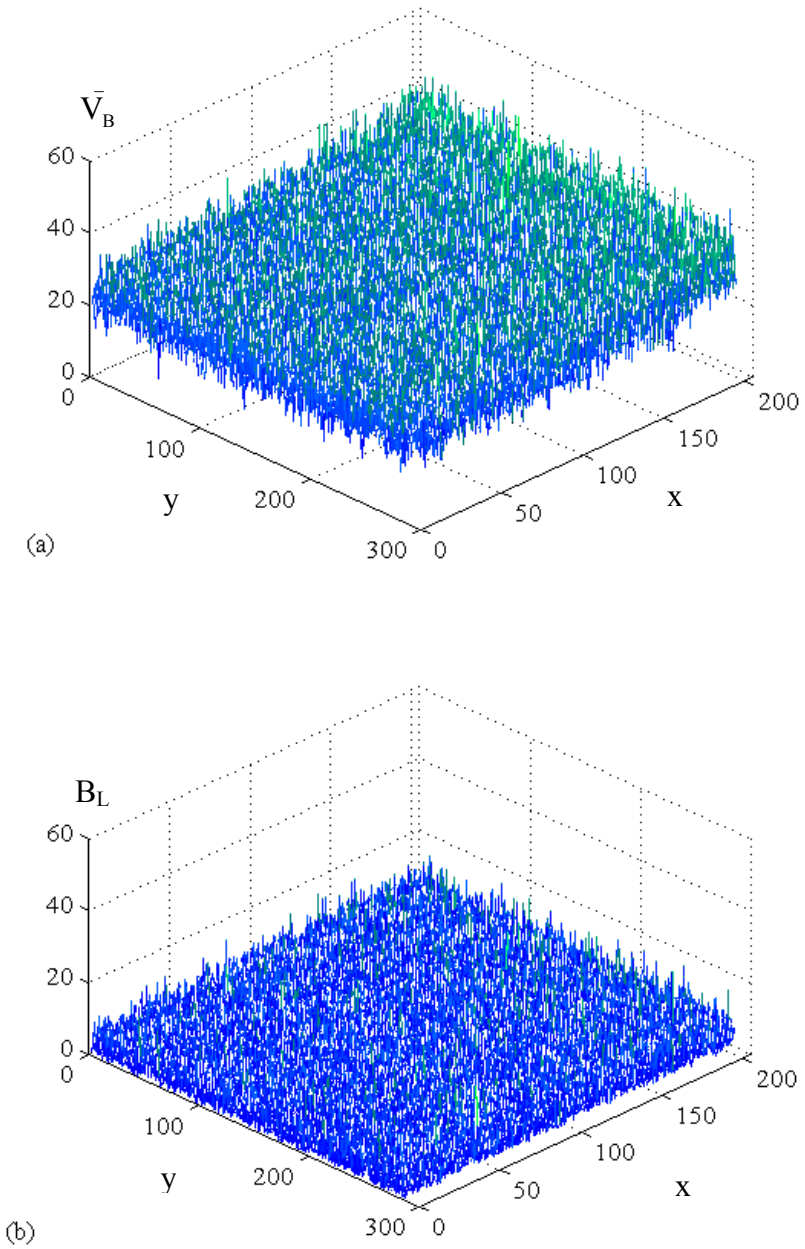

Figure 3.2-7 Dark current on the backward scattering image: (a) before correction, (b) after correction; where *y* is the column index and *x* is the row index.

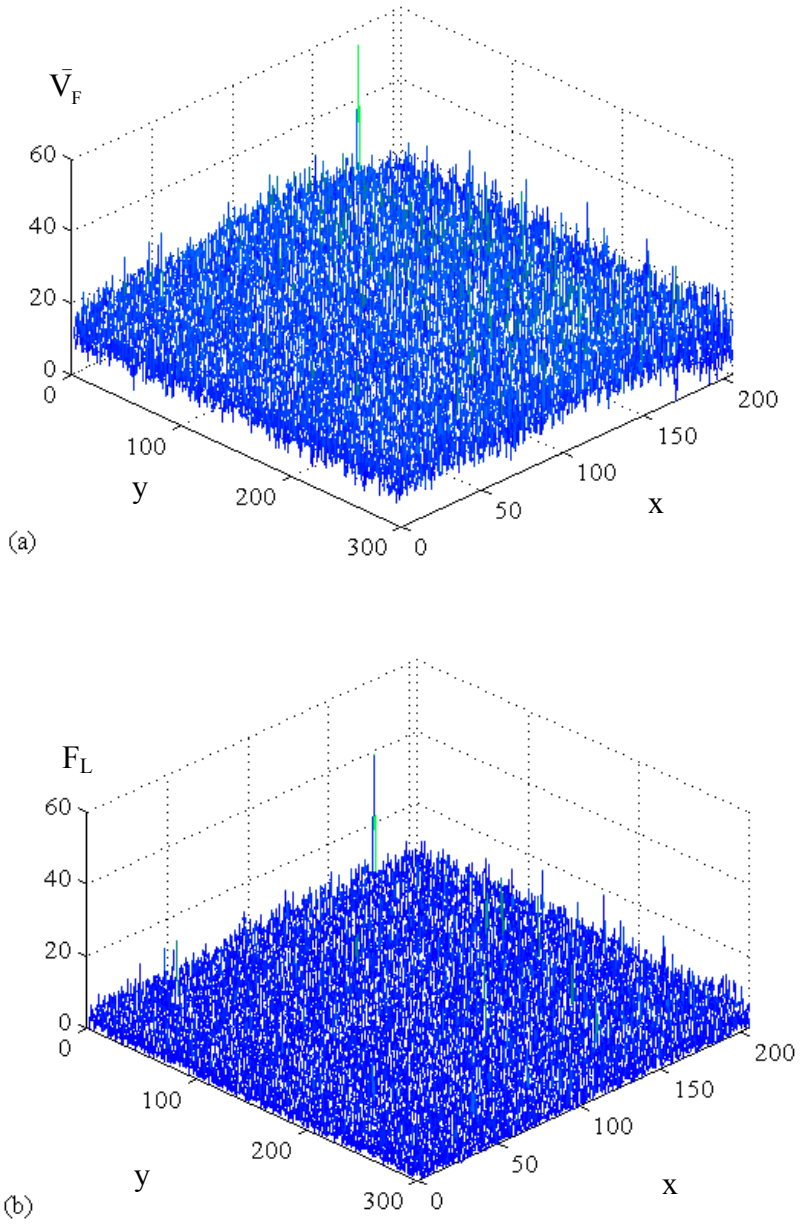

Figure 3.2-8 Dark current on the forward scattering image: (a) before correction, (b) after correction; where *y* is the column index and *x* is the row index.

3.3 Application of the Model

This chapter introduces a prototype x-ray scanning system and its model that will be used throughout the rest of this dissertation. For theoretical analysis and simulations, Algorithm 3.4 is used:

- *Algorithm 3.4*

(i) Use Equation (2.5) to represent the x-ray source;
(ii) Simulate the detected transmission and scatter signals with Equations (3.1), (3.2), and (3.3).

Algorithm 3.5 is used to correct the scanned images for the experimental work.

- *Algorithm 3.5*

(i) Collect images $\bar{V}_T$, $\bar{V}_B$, and $\bar{V}_F$ as shown in Figure 3.2-1;
(ii) Do shading or dark current correction for the measurement data with *Algorithm* 3.2 for transmission images, and *Algorithm* 3.3 for scattering images;
(iii) For above data, apply Equation (3.11) to correct the effect of the amplifier circuit for the interested objects, to obtain estimates of *T*, *B*, and *F* as shown in Figure 3.2-1.

A group of images are given from Figure 3.3-1 to Figure 3.3-6, to show the shading or dark current corrections on backgrounds, and correction of the amplifier circuit effect on foreground. The objects shown in our example are: the overlapped three plastic plates and a thin aluminum plate.

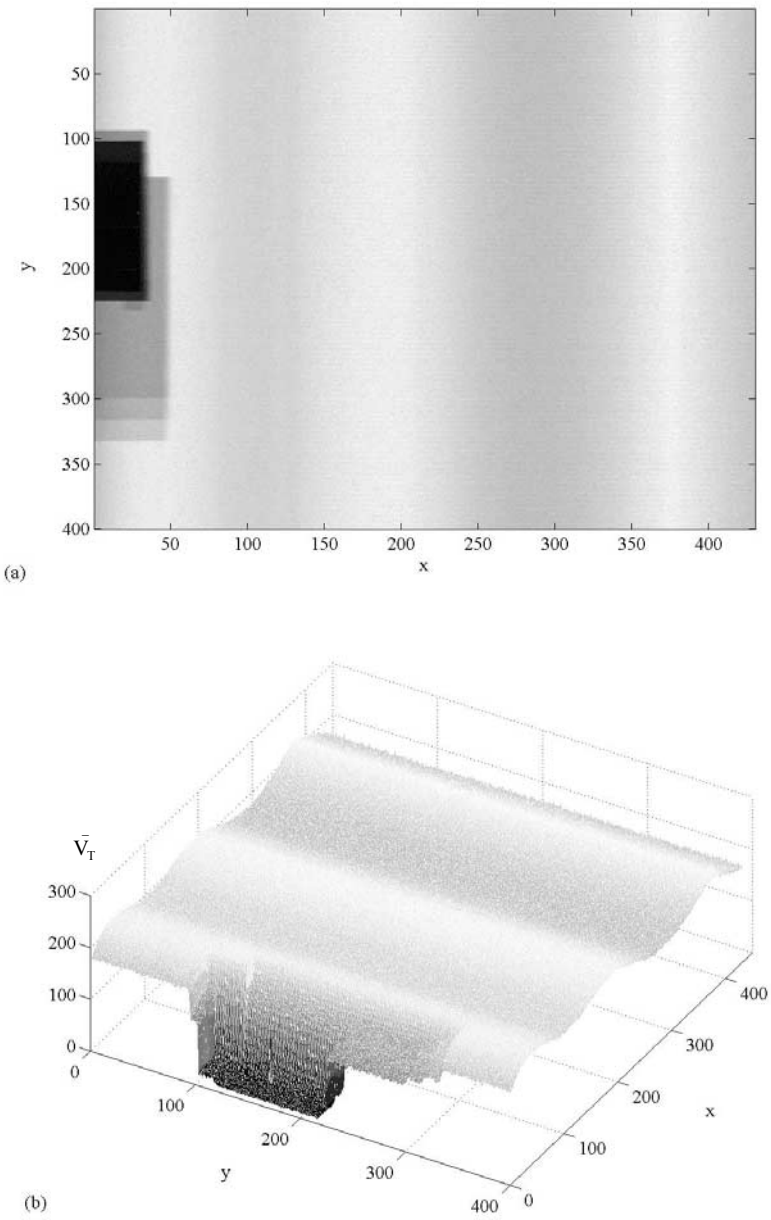

Figure 3.3-1 A transmission image scanned using the prototype scanner. (a) Image $\bar{V}_T$ with non-uniform background. (b) The same image shown as a three-dimensional plot.

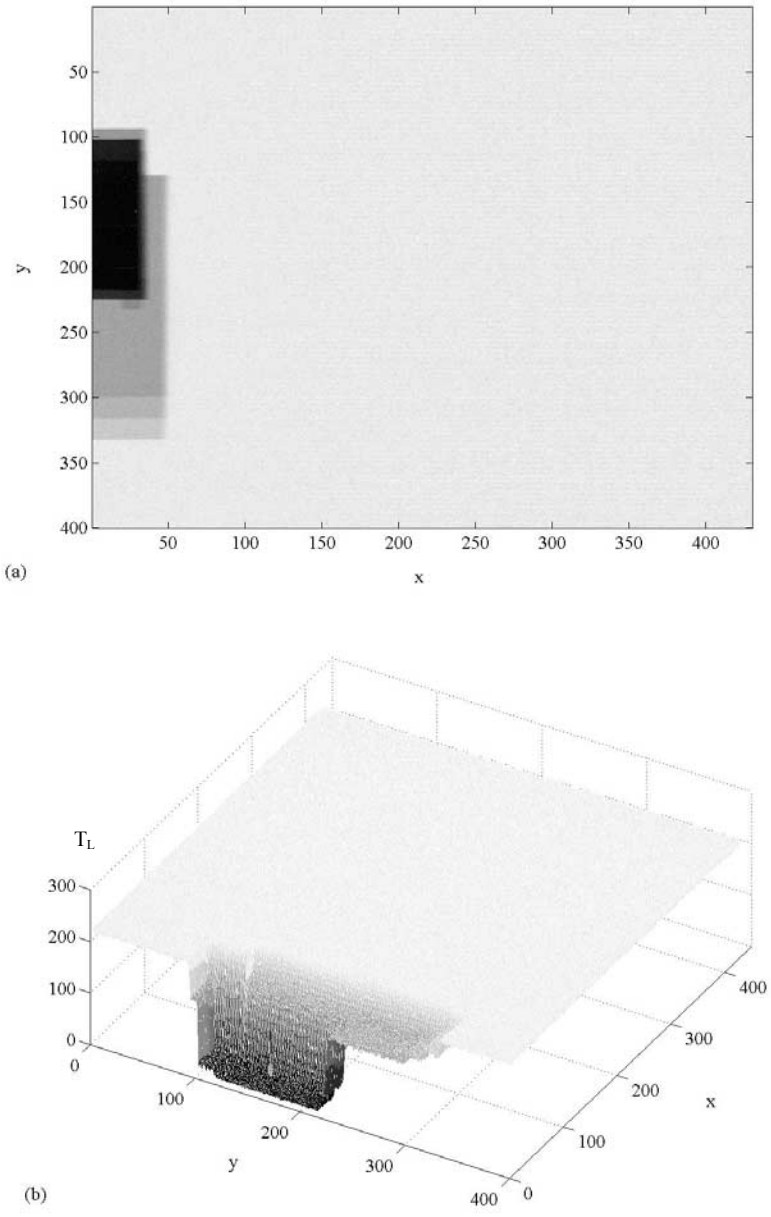

Figure 3.3-2 Transmission image T_L after correction of Figure 3.3-1. (a) Image with an uniform background. (b) The same image shown as a three-dimensional plot.

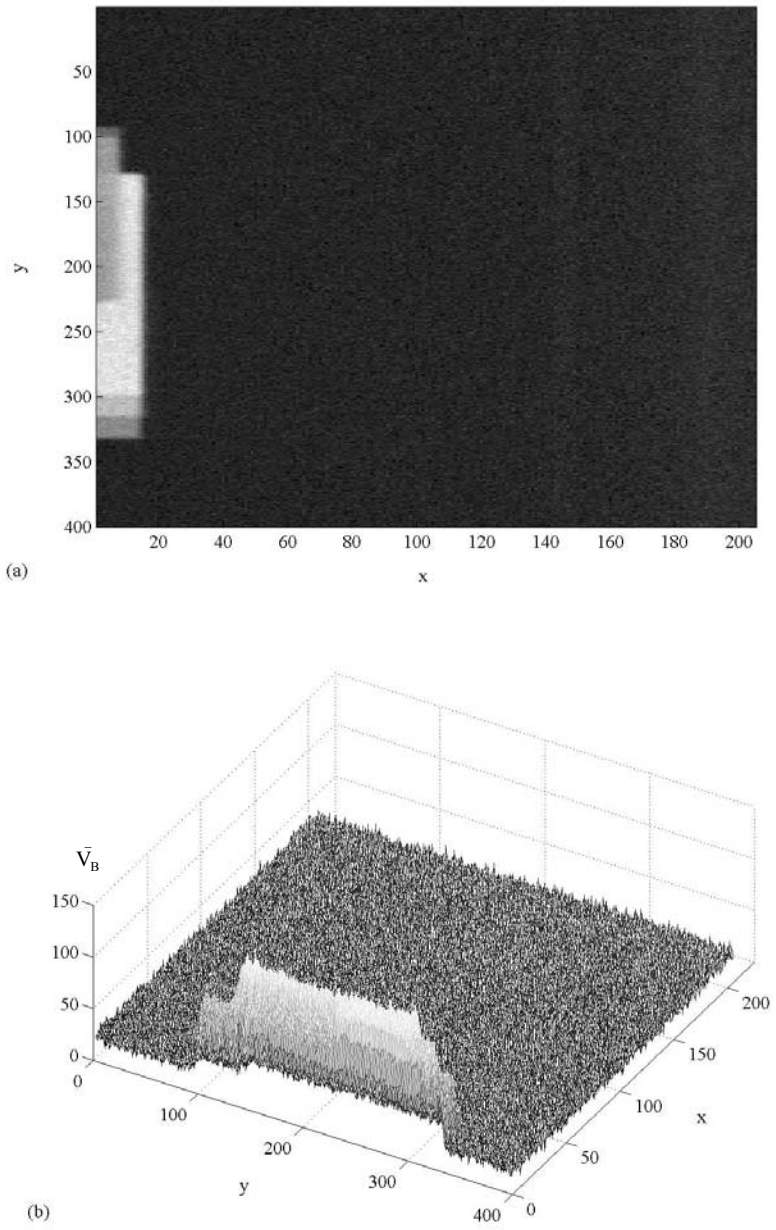

Figure 3.3-3 A backward scatter image scanned using the prototype scanner. (a) Image $\bar{V}_B$ with a dark current. (b) The same image shown as a three-dimensional plot.

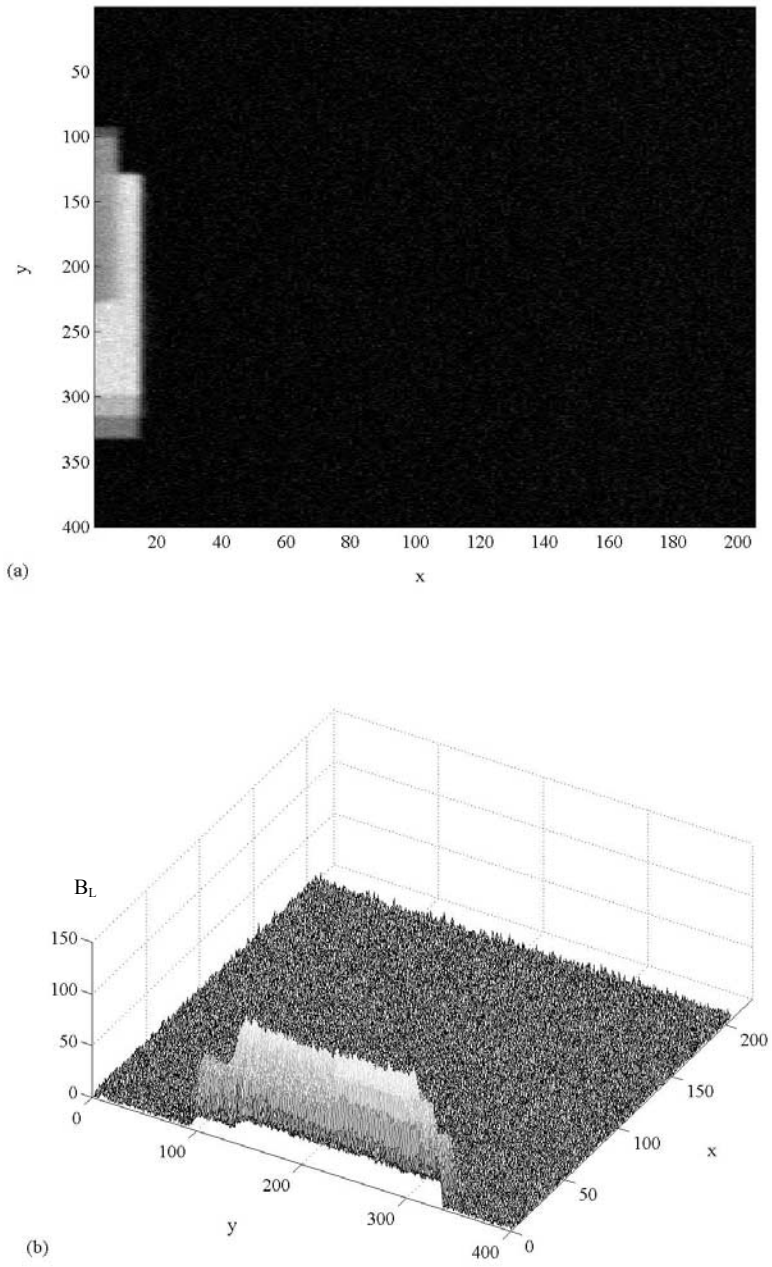

Figure 3.3-4 Backward scatter image after correction of Figure 3.3-3: (a) Image B_L. (b) The same image shown as a three-dimensional plot.

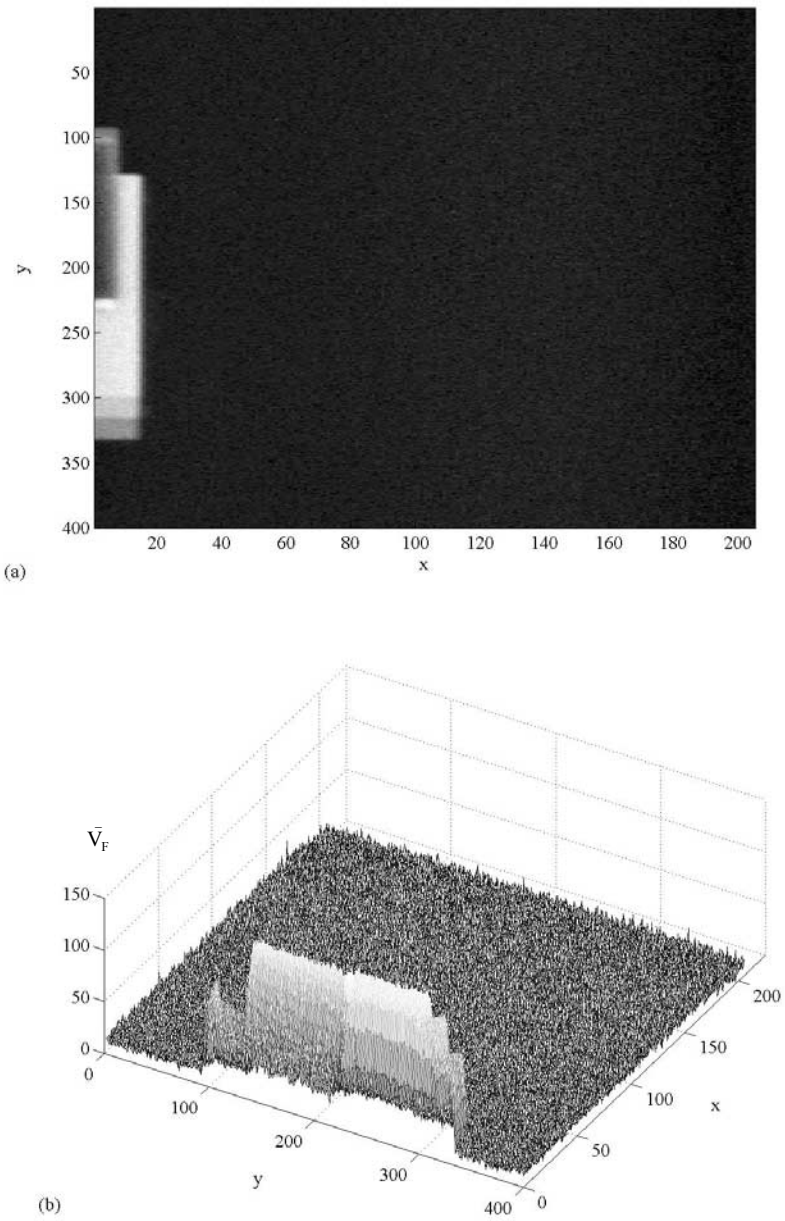

Figure 3.3-5 A forward scatter image scanned using the prototype scanner. (a) Image $\bar{V}_F$ with a dark current. (b) The same image shown as a three-dimensional plot.

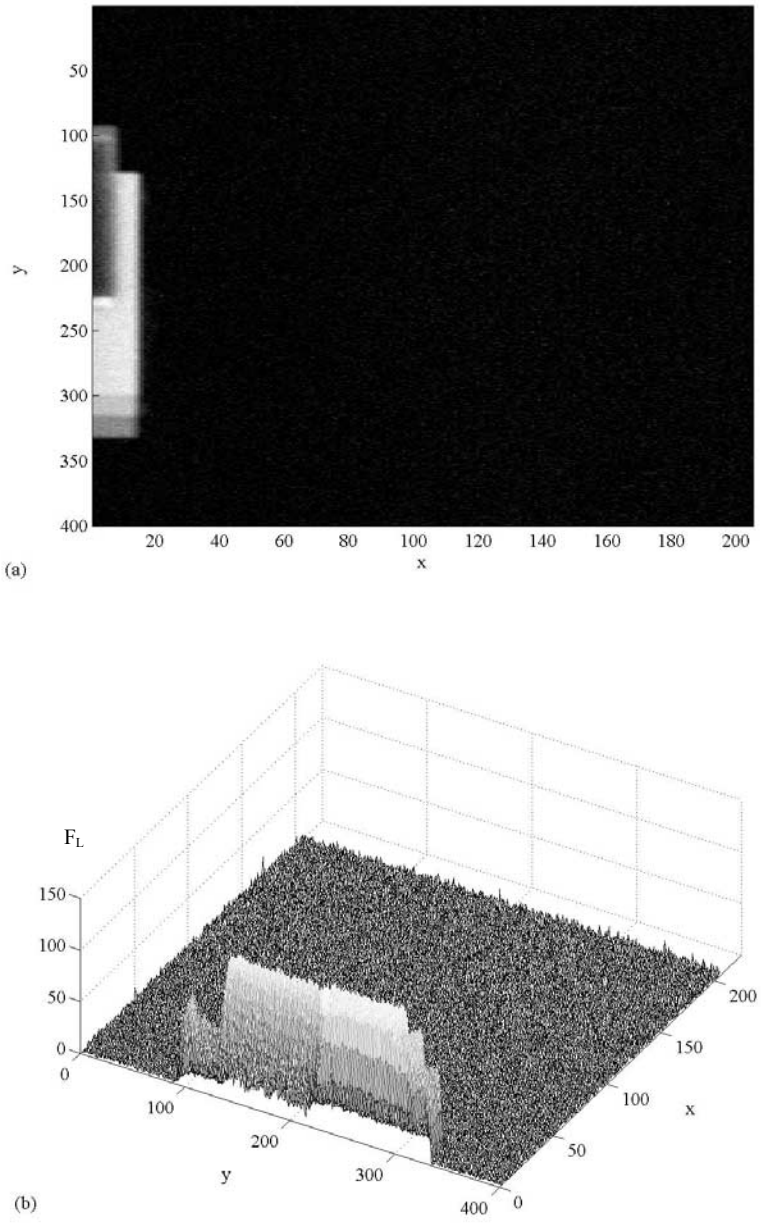

Figure 3.3-6 Forward scatter image after correction of Figure 3.3-5. (a) Image F_L. (b) The same image shown as a three-dimensional plot.